Available online at www.sciencedirect.com
ScienceDirect
Journal of Power Sources 158 (2006) 953–963
JOURNAL OF POWER SOURCES
www.elsevier.com/locate/jpowsour

Impedance-based overcharging and gassing model for VRLA/AGM batteries

M. Thele [a,*], E. Karden [b], E. Surewaard [b], D.U. Sauer [a]

[a] *Electrochemical Energy Conversion and Storage Systems Group, Institute for Power Electronics and Electrical Drives (ISEA), RWTH Aachen University, Jaegerstrasse 17-19, D-52066 Aachen, Germany*
[b] *Ford Motor Company, Germany*

Available online 27 December 2005

Abstract

This paper presents for the first time an impedance-based non-linear model for lead-acid batteries that is applicable in all operational modes. An overcharging model describes the accumulation and depletion of the dissolved Pb^{2+} ions. This physical model has been added to the earlier presented model to expand the model validity. To properly represent the charge acceptance during dynamic operation, a concept of "hardening crystals" has been introduced in the model. Moreover, a detailed gassing and oxygen recombination model has been integrated. A realistic simulation of the overcharging behavior is now possible. The mathematical description is given in the paper. Simplifications are introduced that allow for an efficient implementation and for model parameterization in the time domain. A comparison between experimental data and simulation results demonstrates the achieved accuracy.

The model enhancement is of major importance to analyze charging strategies especially in partial-cycling operation with limited charging time, e.g. in electrically assisted or hybrid cars and autonomous power supply systems.

Keywords: Impedance spectroscopy; Modeling; Overcharging; Valve-regulated; Lead-acid; Regenerative braking

1. Introduction

The analysis of operation strategies (e.g. in electrically assisted or hybrid cars and autonomous power supply systems) needs dynamical simulation models for lead-acid batteries as an important prerequisite. Since these batteries are non-linear and highly dependent on divers parameters like temperature, state of charge (SOC) and short-term history [8,10], the implementation of these models is very difficult and a simple modeling with high precision is consequently nearly impossible. However, fast computing and small parameterization effort are mainly asked.

Electrochemical impedance spectroscopy (EIS) is an adequate tool for the development and the parameterization of battery simulation models considering these aspects. Small-signal excitation and the evaluation of the system's response enable accurate investigation at nearly any working point. The computing and simulation effort of an impedance-based model can be very small compared with physically or chemically based models. The core of our impedance-based model consists of elements that are related to physico-chemical processes. These processes are modeled in terms of inductors, capacitors and resistors with non-linear dependency on temperature, SOC and battery current [1,2].

Similar impedance-based modeling approaches have been presented recently by several groups [11–15]. Barsoukov et al. [12] and Buller [13] demonstrated the applicability of this approach to several battery technologies by using non-linear equivalent-electrical-circuit models. Andersson et al. [14] analyzed impedance data by a model for porous electrodes to deduce physical parameters, namely the porosity and the active surface of the electrodes. For state of charge diagnosis of lead-acid batteries, the approach is employed by Salkind et al. [15] and Abolhasani et al. [16], however, by using linearized models that strongly limit the validity range of the diagnosis. Formerly, Mauracher and Karden [11] also proved the possibilities of this approach using a highly non-linear model whereby the validity range was limited to the range of 10–90% SOC. Additionally, the model was limited to moderate charging currents.

* Corresponding author. Tel.: +49 241 8096945.
E-mail address: te@isea.rwth-aachen.de (M. Thele).
URL: http://www.isea.rwth-aachen.de.

0378-7753/$ – see front matter © 2005 Elsevier B.V. All rights reserved.
doi:10.1016/j.jpowsour.2005.11.025

Nomenclature

c	actual ion concentration (mol m^{-3})
c_s	equilibrium ion concentration (mol m^{-3})
D	diffusion constant (m^2 s^{-1})
D_{eff}	effective parameter incl. diffusion constant (s^{-1})
$E_{Pb^{2+}}$	overvoltage at negative electrode (V)
$E_{Pb^{2+}pos}$	overvoltage at positive electrode (V)
f	radii distribution of crystals (m^{-4})
F	Faraday constant (96485.34) (C mol^{-1})
$\hat{I}$	current density (A m^{-3})
I_{0,H_2}	exchange current negative electrode (A)
I_{0,O_2}	exchange current positive electrode (A)
$I_{gas,neg}$	gassing current negative electrode (A)
$I_{gas,pos}$	gassing current positive electrode (A)
I_{recom}	recombination current (A)
$k_{hardening}$	linear scaling factor "hardening crystals"
K	amount of discharged (A s)
n	valence Pb^{2+} (2)
n_{new}	total number of not hardened crystals (mol m^{-3})
N	number of $PbSO_4$ crystals (m^{-4})
q	rate of ions per time due to electrochemical process (mol m^{-3} s^{-1})
$q_{hardening}$	rate of hardened crystals (mol m^{-3} s^{-1})
q_{new}	rate of not hardened crystals (mol m^{-3} s^{-1})
r	radius of $PbSO_4$ crystal (m)
R	gas constant (8.314472) (J mol^{-1} K^{-1})
s	rate of ions per time due to chemical process (mol m^{-3} s^{-1})
T	temperature (K)
U_T	temperature voltage (V)
V_{PbSO_4}	total volume of $PbSO_4$ (m^3 m^{-3})
x_0	median radius (m)
Z	number of crystals with median radius (m^{-4})

Greek letters

α_{O_2}	symmetric coefficient
η	overvoltage (V)
σ	dispersion of radii distribution (m)
$\tau_{hardening}$	time constant of hardening process (s)
τ_{recom}	time constant of recombination process (s)
υ_m	molar volume $PbSO_4$ (48.22×10^{-6}) (m^3 mol^{-1})

In order to enlarge the validity range of this modeling approach, this paper presents a significant improvement. An overcharging model and a more sophisticated gassing model have been employed to enable the analysis of the charging behavior of the battery, which is of particular importance during cyclic operation with limited charging time. The implementation and parameterization have been enabled by reference-electrode measurements inside a valve-regulated lead-acid (VRLA) battery. Thereby, investigations on the dynamic behavior of each electrode have been also made possible and will be additionally illustrated in this paper.

Without an overcharging model, the model output can deviate significantly from the measurement during charging periods. This limitation is inherent to the impedance method, because the battery response is subject to a Fourier analysis during the impedance measurement. This analysis demands a constant or at most a time-dependent (approximately) linear shift of the dc-response, which is not given in case overcharging effects occur. Consequently, these effects are not accessible for the impedance method and are thus not covered by the impedance-based model without an additional overcharging model. Hence, the original model significantly underestimated battery voltage when applying charging currents at high states of charge or even at medium states of charge if a high charging current was applied. The model validity ends where the processes cannot be described simply by the Butler–Volmer process and the accumulation of acid concentration in the porous active material. The charge acceptance of the battery model (without overcharging model) was accordingly much too high during voltage limited charging periods.

As an additional process, which is identified to be the limiting process during charging at high currents rates or high states of charge, the employed overcharging model describes the consumption of Pb^{2+} ions. The Pb^{2+} ion concentration decreases during charging caused by the generation of Pb and PbO_2 from Pb^{2+} ions. A liquid phase process is assumed here. The dissolution process of the $PbSO_4$ crystals limits Pb^{2+} ion delivery and finally the charge acceptance of the battery. During operation at moderate current rates and low state of charge, the dissolution rate of $PbSO_4$ crystals is high and, consequently, it is not recognized as a limiting process.

A further process needs to be recognized which becomes obvious during extended experimental tests with lead-acid batteries. If a battery undergoes shallow cycles around a fixed state of charge, the charge acceptance is increasing with increased cycling time. This leads to the assumption that the newly formed sulfate crystals can be dissolved during charging easier than sulfate crystals that have been formed longer time ago. This has been taken into account in the model by using a concept of "hardening crystals". Hereby, crystals that have been formed recently have a higher dissolution rate than older crystals.

The employment of the detailed gassing model enables the description of the gassing processes at the negative and positive electrode. In addition, the recombination process at the negative electrode inside a VRLA battery can be simulated. Thus, the charge efficiency of the battery can be calculated by regarding the negative and positive gassing currents with respect to the terminal current. Moreover, the depolarization of the negative electrode can be simulated which is forced by the recombination process.

The enhanced model yields high precision in predicting the electrical battery performance even if high charging currents are applied to the battery. The parameterization and validation of the model has been carried out for a JCI Optima Red Top VRLA battery (44 Ah, 12 V). The same approach can be also employed for flooded lead-acid batteries or prismatic AGM batteries. Generally, the same approach should be also applicable for VRLA/Gel batteries, but this has not been tested so far.

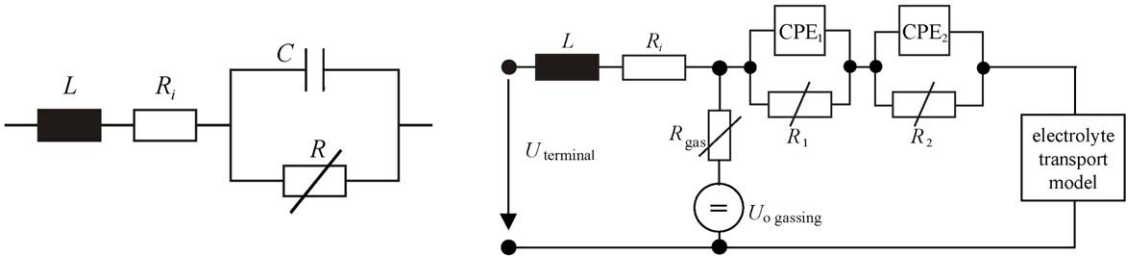

Fig. 1. Equivalent circuit of a battery half-cell (left hand); equivalent circuit for a complete lead-acid battery cell (right hand) [2].

2. The impedance-based modeling approach

For a basic modeling approach, a slightly simplified Randles equivalent-circuit can be employed ([8]; Fig. 1, left hand). The equivalent circuit is valid for both battery electrodes with differing parameters. It consists of an internal resistance R_i, an inductance L, a capacitance C and a non-linear resistance R. L is mainly caused by the metallic connectors between the terminals and the electrodes of the battery. The ohmic resistance R_i is due to the limited conductance of the contacts, the inter-cell connections, the grids, the active masses and the electrolyte. R_i depends on SOC, age and temperature of the battery. The parallel connection of the capacitance C and the non-linear resistance R represents the double layer capacity and the charge transfer resistance.

An equivalent circuit for a complete battery cell can be obtained by a series connection of two Randles circuits. A few modifications [1,2] have been employed for the impedance-based lead-acid battery model, namely generalized capacitive elements (CPE: constant phase element [9]), an electrolyte transport model (calculation of the OCV and the diffusion overpotential) and a parallel current path for gassing as the main side reaction.

For the model improvement presented in this paper, the equivalent circuit has been modified significantly. The new circuit considers all mentioned physico-chemical processes including the overcharging limitations and side reactions.

3. Overcharging process in lead-acid batteries

3.1. Processes to be modeled

The overall process of a lead-acid battery can be subdivided into three different reactions (Fig. 2):

1. Electrochemical process: The rate depends only on the current given by the terminal current. During discharging, each pair of electrons is transferred to or from a dissolved Pb^{2+} ion which is released into the electrolyte.
2. Diffusion process: The electrical charge of each Pb^{2+} ion must be counterbalanced by anions like SO_4^{2-} or HSO_4^{-}.
3. Chemical process: The $PbSO_4$ molecules undergo a crystallization process and form $PbSO_4$ crystals.

During charging, the process is reversed. Proportional to the charging current, the electrochemical process consumes a Pb^{2+} ion flow. The diffusion process supports these ions to the reaction site. Caused by the depletion of the Pb^{2+} ion concentration, the $PbSO_4$ crystals are dissolving [3,4].

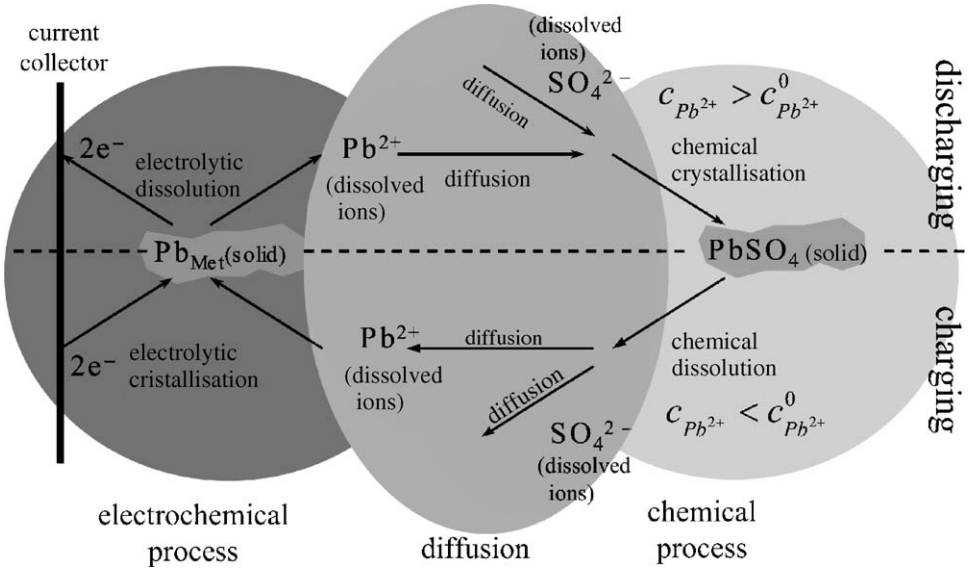

Fig. 2. Schematic of the charge and discharge reaction on a microscopic level in the negative electrode.

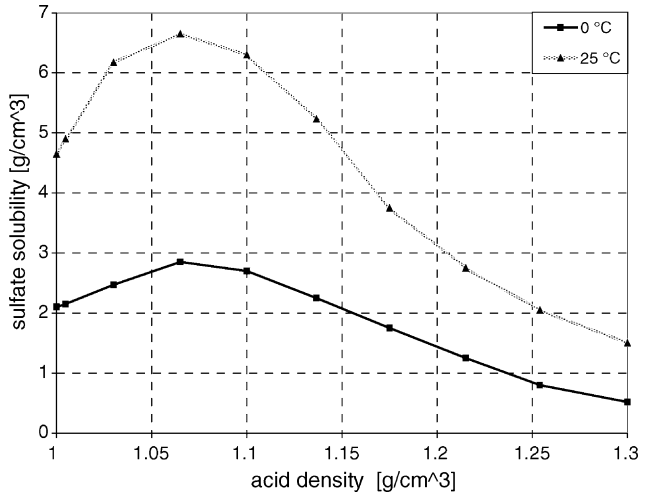

Fig. 3. Solubility of sulfate in sulfuric acid for different acid concentrations and temperatures [10] using stepwise linear interpolation.

Assuming a battery current above zero (charging), ions are consumed and can be delivered by the dissolution process of $PbSO_4$ crystals only (Fig. 3). Thus, the ratio of the actual ion concentration c and c_s (equilibrium concentration, function of temperature and acid concentration) is below unity, and consequently, according to basic electrochemical laws, additional overvoltages occur (see Eqs. (1) and (2)).

$$\text{positive electrode}: \quad E_{Pb^{2+}pos} = -\frac{RT}{nF}\ln\left(\frac{c}{c_s}\right) \tag{1}$$

$$\text{negative electrode}: \quad E_{Pb^{2+}neg} = \frac{RT}{nF}\ln\left(\frac{c}{c_s}\right) \tag{2}$$

During discharging, Pb^{2+} ions will be produced by the electrochemical reaction. The ion concentration c will increase due to the limited crystallization process of the $PbSO_4$ crystals. However, due to the logarithmic behavior, the overvoltages will change significantly slower during discharging compared with charging. The only significant impact of the Pb^{2+} ion concentration during discharging can be observed as the "coup de fouet" or "Spannungssack" because the chemical process is suppressed at the beginning of a discharge process if no sulfate crystal seeds are present already. This is the case, if the battery has been very well charged beforehand. A "coup de fouet" is the more pronounced, the better the previous charging has been.

According to the illustrated effects, the changing of the concentration c with time can be explained by the following equation. The description of the processes and the mathematics follow the work of Kappus [4] and its adaptation for simulation models by Sauer [7].

$$\dot{c} = q - s \tag{3}$$

The rate q is given in $\mathrm{mol\,(m^3 s)^{-1}}$ and corresponds to the consumed or generated Pb^{2+} ions due to the electrochemical process per time (related to an unified volume V_{uni}) and is proportional to the main reaction current. s is the number of ions that are dissolved or crystallized from the $PbSO_4$ crystals within the chemical process step. q can be calculated by Eq. (4) with I as a current density per volume V_{uni}, F is the Faraday constant. The Eqs. (3) and (4) are valid for both electrodes.

$$q = \frac{I}{2F} \tag{4}$$

s can be calculated according to:

$$s = \frac{\mathrm{d}}{\mathrm{d}t}\left(\frac{4\pi}{3\upsilon_m}\int_{r_{min}}^{r_{max}} r^3 f(r,t)\,\mathrm{d}r'\right) \tag{5}$$

where r is the radius of the lead-sulfate crystals, $f(r)$ is the radii distribution function of the lead-sulfate crystals, υ_m is the molar volume of lead sulfate, and r_{min} and r_{max} define the range of available crystal sizes. Assuming an approximately time independent radii distribution of the $PbSO_4$ crystals ($f(r, t) \approx f(r)$) for small time steps, the equation simplifies to:

$$s = \frac{4\pi}{3\upsilon_m}\int_{r_{min}}^{r_{max}} \frac{\mathrm{d}}{\mathrm{d}t}(r^3) f(r)\,\mathrm{d}r' = \frac{4\pi}{\upsilon_m}\int_{r_{min}}^{r_{max}} r^2 \dot{r} f(r)\,\mathrm{d}r' \tag{6}$$

The distribution $f(r)$ corresponds to the number of crystals of each radius per volume V_{uni}. The speed of radius change $\dot{r}$ can be calculated by:

$$\dot{r} = \frac{\upsilon_m D(c - \tilde{c}(r))}{r} \tag{7}$$

with D as a diffusion constant, c_s the equilibrium concentration of Pb^{2+} ions in sulfuric acid with infinite radius r and c the actual concentration of the Pb^{2+} ions in the electrolyte according to Eq. (3). The dependency of c_s on the crystal radius makes Eq. (7) very difficult to solve. However, during normal charge and discharge operation the impact of the dependency of c_s on the crystal radius is of no relevance, therefore it is not taken into account here.[1] Consequently, Eq. (6) simplifies to (with $\tilde{c}(r) \approx c_s$):

$$s = 4\pi D(c - c_s)\int_{r_{min}}^{r_{max}} r f(r)\,\mathrm{d}r' \tag{8}$$

The total volume of $PbSO_4$ V_{PbSO_4} (related to V_{uni}) depends on the SOC of each electrode and is consequently known from the Ah balance taking into account the gassing current. K corresponds to the discharged Ahs (related to V_{uni}) and becomes zero for a fully charged electrode (no sulfate crystals left).

$$V_{PbSO_4} = \frac{4\pi}{3}\int_{r_{min}}^{r_{max}} r^3 f(r)\,\mathrm{d}r' = \frac{K}{2F}\upsilon_m \tag{9}$$

[1] Nevertheless, the dependency of c_s from r, which can be described by the equation $\tilde{c}(r) = c_s e^{(2\sigma\upsilon_m/RTr)}$ (assuming the validity of the Gibbs–Thomson-relationship) is very important if recrystallization processes during open circuit conditions of the battery should be taken into account. Crystals with small radius tend to dissolve while crystals with large radius tend to grow. As a result, the average sulfate crystal radius is increasing. This processes is accelerated with increasing temperature and with increasing Pb^{2+} solubility (and therefore low states of charge as shown in Fig. 3). This process must be taken into account for aging models but this is out of the scope of the model under discussion in this paper.

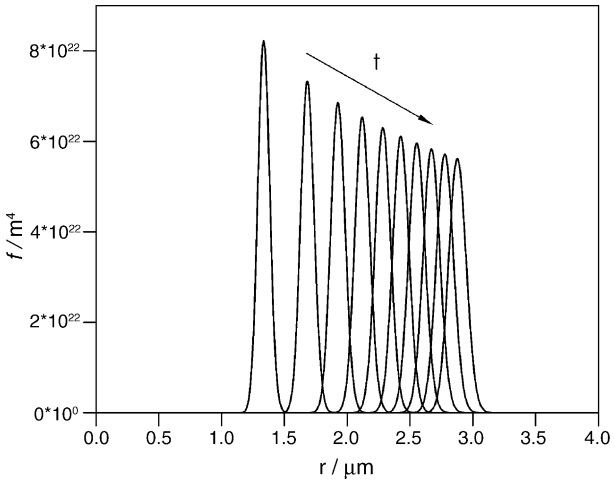

Fig. 4. Calculated size distribution $f(r)$ of lead-sulfate crystals during discharging using the I_{10} based on a full mathematical approach (published in [7]).

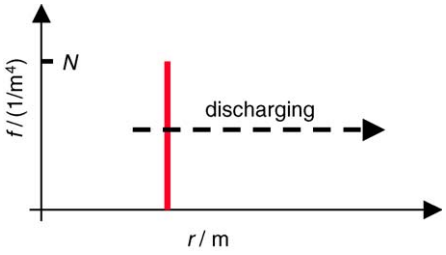

Fig. 5. Simplest distribution of the crystals radii with constant number of crystals N and SOC dependent radius r.

3.2. Modeling the overcharging process

The model development requires some simplifications of the overcharging theory. Namely, the size distribution $f(r)$ of the lead-sulfate crystals has to be approximated.[2] Three different modeling approaches have been tested and the most suitable assumption with an easy implementation and less parameterization effort has been chosen finally. A realistic distribution is illustrated in Fig. 4 which has been calculated based on a full mathematical model using the 10 h current I_{10}. The full model unfortunately takes very long computation time and the implementation is very difficult.

3.2.1. Equal radius of all crystals

The simplest approximation of a crystal-size distribution is the assumption of a fixed number of N crystals with equal radius r ($f(r) = N$). The radius consequently depends on the total $PbSO_4$ volume and, thus, depends on SOC ($r = f(N, \mathrm{SOC})$). The radius becomes zero for a fully charged electrode and increases during discharging (Fig. 5).

Using this approximation, Eq. (5) simplifies to:

$$s = \frac{\mathrm{d}}{\mathrm{d}t}\left(\frac{4\pi}{3\upsilon_\mathrm{m}}Nr^3\right) = \frac{4\pi}{\upsilon_\mathrm{m}}Nr^2\dot{r} = 4\pi NrD(c - c_\mathrm{s}) \tag{10}$$

[2] Generally it is possible to solve the equation with numerical methods. This has been demonstrated by Sauer in [7]. However, the numerical solution of the full equation is very difficult and consumes much computing time.

Eq. (9) simplifies to:

$$V_{\mathrm{PbSO_4}} = \frac{4\pi}{3}Nr^3 = \frac{K}{2F}\upsilon_\mathrm{m} \tag{11}$$

$$\Rightarrow r = \sqrt[3]{\frac{K}{nF}\upsilon_\mathrm{m}\frac{3}{N4\pi}} \tag{12}$$

Considering Eqs. (4), (10) and (12), Eq. (3) can be written as:

$$\dot{c} = \frac{I}{2F} - D(c - c_\mathrm{s})\sqrt[3]{\frac{K}{nF}\upsilon_\mathrm{m}3 \times 4^2N^2\pi^2} \tag{13}$$

3.2.2. Triangular distribution

To reproduce the above shown realistic distribution (Fig. 6), a triangular distribution with a medium radius x_0 and a dispersion σ has been employed for modeling the overcharging processes. Z accords to the number of crystals with medium radius. Three cases have to be distinguished:

1. The medium radius x_0 is higher than the dispersion σ. The triangular distribution $f(r)$ moves with decreasing x_0 and constant σ to smaller radii during charging (see Fig. 6, left hand). The number of crystals with medium radius is kept fixed.
2. The medium radius x_0 is smaller than the dispersion σ but greater than zero. The triangular distribution $f(r)$ moves with decreasing x_0 to smaller radii during charging, the "left side" of the triangle is cut by the ordinate and the number of crystals is decreasing (Fig. 6, middle).
3. In case the medium radius x_0 reaches zero during charging, the condition $x_0 = 0$ and a constant dispersion is assumed. Solely, the maximum number Z_max decreases further during charging.

For case 1, the following equations can be found regarding Eqs. (8) and (9). To solve Eq. (15), the median radius x_0 has to be determined numerically using Eq. (14).

$$V_{\mathrm{PbSO_4}} = \frac{4\pi}{3}Z\left(\sigma x_0^3 + \frac{1}{2}\sigma^3 x_0\right) \tag{14}$$

$$s = 4\pi D(c - c_0)Zx_0\sigma \tag{15}$$

The corresponding equations for case 2 are (a numerical solver is needed again):

$$V_{\mathrm{PbSO_4}} = \frac{4\pi}{3}\frac{Z}{\sigma}\left(\frac{(\sigma + x_0)^5}{20} - \frac{1}{10}x_0^5\right) \tag{16}$$

$$s = 4\pi D(c - c_0)\frac{Z}{\sigma}\left[\frac{1}{6}(x_0 + \sigma)^3 - \frac{2}{6}x_0^3\right] \tag{17}$$

Case 3 gives the following equations at which no numerical solvers are necessary:

$$V_{\mathrm{PbSO_4}} = \tfrac{1}{15}\pi\sigma^4 Z_\mathrm{max} \tag{18}$$

$$s = \tfrac{2}{3}\pi D(c - c_0)Z_\mathrm{max}\sigma^2 \tag{19}$$

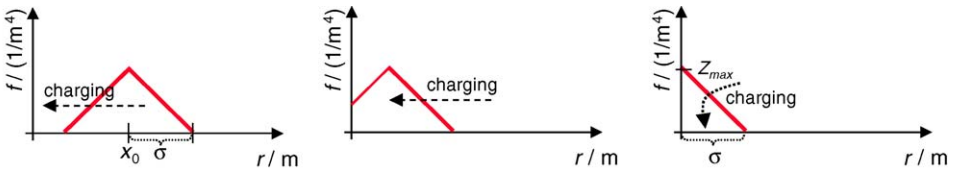

Fig. 6. Triangular distribution of the crystal size, shift of median radius x_0 during charging, Z_{max} decreases if $x_0 = 0$ and σ remains constant (right hand figure).

3.2.3. Ramp distribution

At higher states of charge, only the third case (Eqs. (18) and (19)) appears. Consequently, the behavior of an overcharging model which considers only this case does not differ from a model using the complete triangular distribution. The implementation (Eq. (20)) is very easy and the parameterization effort can be simplified by only one effective parameter D_{eff}. Consequently, the ramp distribution has been employed. All subsequent results are based on this approach. Eq. (20) is derived from Eqs. (18) and (19), no empirical assumptions are included.

$$s = 10(c - c_0)V_{\text{PbSO}_4}\frac{D}{\sigma^2} = 10(c - c_0)V_{\text{PbSO}_4}D_{\text{eff}} \tag{20}$$

3.3. Concept of "Hardening Crystals"

The model implementation described so far yields an overcharging model that uniquely depends on SOC. However, if a battery undergoes shallow cycling, the charge acceptance is increasing with increased cycling time even though the SOC is approximately stable. The $PbSO_4$ crystals that have been formed recently appear to have a higher dissolution rate than older crystals.

A model modification that includes the effects of the battery current in short-term history has been employed. The rate of the new (not yet hardened) crystals q_{new} is proportional to the difference of the main reaction current $-I$ and the rate of the hardening crystals $q_{\text{hardening}}$ (Eq. (21)). The actual number of the recently formed crystals corresponds to the integrated value of the rate q_{new} (Eq. (22)). The higher n_{new} the higher is the charge acceptance of the battery whereat n_{new} is limited to positive values.

$$q_{\text{new}} = -\frac{I}{2F} - q_{\text{hardening}} \tag{21}$$

$$n_{\text{new}} = \int q_{\text{new}}\,\mathrm{d}t \tag{22}$$

A *RC*-element has been employed to model this correlation (Fig. 7). The balancing (Eq. (21)) corresponds to the nodal equation and the number n_{new} corresponds to the charge Q_C of the capacitor. The time constant $\tau = RC$ determines the hardening time of the crystals. The variable solubility of the crystals is considered by Eq. (23) using a slightly modified parameter D_{eff} (compare Section 3.2.3). Thus, two parameters (t and $k_{\text{hardening}}$) have to be determined by simple parameter identification.

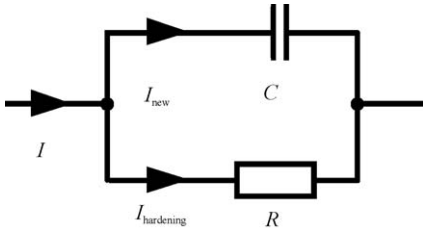

Fig. 7. Implementation of the "hardening crystals" modeling approach.

$$D_{\text{hardening}} = (1 + (k_{\text{hardening}}n_{\text{new}}))D_{\text{eff}} \tag{23}$$

4. Secondary reactions in VRLA batteries

4.1. Processes to be modeled

Four secondary reactions are characteristic for a lead-acid system:

1. Oxygen evolution at the positive electrode
2. Hydrogen evolution at the negative electrode
3. Oxygen reduction at the negative electrode
4. Grid corrosion at the positive electrode

The first two reactions can both be described by the Tafel equations.

$$I_{\text{gas,pos}} = I_{0,\text{O}_2}\exp\left(\frac{n\alpha_{\text{O}_2}\eta}{U_T}\right) \tag{24}$$

$$I_{\text{gas,neg}} = I_{0,\text{H}_2}\exp\left(\frac{-n(1-\alpha_{H_2})\eta}{U_T}\right) \tag{25}$$

The overvoltage η represents the difference between the equilibrium potential of the respective secondary reaction and the present potential of the involved electrode. The constants are exchange current I_{0,O_2} and I_{0,H_2}, number of transferred elementary charges n, symmetric coefficients α_{O_2} and α_{H_2} and the temperature T ($(RT)/F \approx 26$ mV if $T = 298$ K).

The typical changes of the overpotential per current decade are -120 and 80 mV for hydrogen and oxygen evolution for flooded lead-acid batteries. In VRLA batteries, an internal oxygen-cycle characterizes the overcharging and float-charging situation. Small gas channels inside the electrolyte allow gas-phase transport of oxygen to the negative electrode where it is reduced (3). As a consequence of the oxygen reduction, hydrogen evolution is largely suppressed and the overcharge voltage is mainly determined by the positive electrode. However, a certain evolution of hydrogen at the negative electrode and grid corrosion at the positive electrode will always be present, e.g. due to the gas transport limitation inside the separator. [1,5,6]

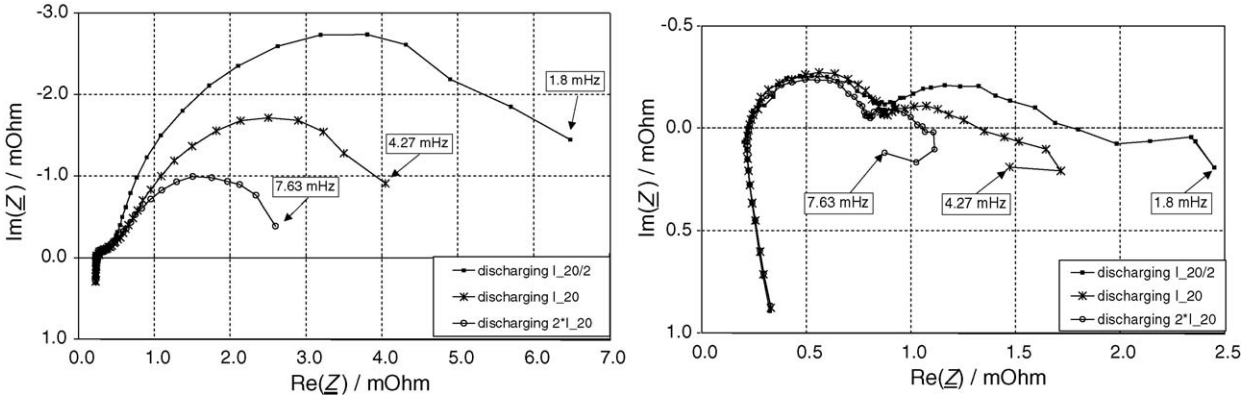

Fig. 8. Impedance measurements of positive (left hand) and negative (right hand) electrode at 70% SOC and room temperature using different dc-currents.

4.2. Modeling the secondary reactions in VRLA batteries

The previous model topology (see Fig. 1, right hand) was characterized by a parallel gassing branch which combined the hydrogen and oxygen evolution.

The introduction and the parameterization of a more detailed topology (Fig. 10) has been made possible by reference-electrode measurements (inside a VRLA battery) which allow separated investigations of the electrodes. The gas evolution can be modeled according to Eqs. (21) and (22) and the oxygen recombination is modeled by a current sink. The recombination current depends on the amount of oxygen which reaches the negative electrode. Moreover, the maximum recombination current is limited due to the limited gas-transport ability inside the AGM separator. The effects of corrosion are neglected.

A phenomenological modeling approach has been applied to determine the recombination current i_{recom} (see Fig. 10). Therefore, a simple parallel *RC*-element has been employed, which cumulates the generated oxygen in terms of a charged capacitor C. The capacitor can be discharged by i_R due to the parallel connected resistor R, the time constant $\tau_{\text{recom}} = R_{\text{recom}} C_{\text{recom}}$ describes the time for the gas transport through the separator. i_R is taken as the recombination current ($i_R = i_{\text{recom}}$). Finally, the maximum recombination current is limited to $i_{\text{recom,max}}$. If $i_R > i_{\text{recom,max}}$, the current surplus $i = i_R - i_{\text{recom,max}}$ corresponds to an excessive amount of generated oxygen which will be blown off by the battery valves. This mode of operation can occur during high rate charging or at high temperatures and should be prevented since water loss is caused which leads to a reduced service life of the battery. $i_{\text{recom,max}}$ can change during the lifetime of a battery. It is very low for a brand new battery because only a small number of gas pores is available. Within increasing loss of water, the number of gas channels increases and therefore $i_{\text{recom,max}}$ increases as well.

5. The improved battery model

5.1. Model structure

Reference-electrode measurements allowed also separated impedance measurements on the electrodes whose results are depicted in Fig. 8. Both, the positive electrode and the negative electrode are characterized by a non-linear current-dependent dynamic behavior.

The positive impedance shows a small current-independent semi-circle for high measurement frequencies f_{ac} and, for increased f_{ac}, a second significant larger current-dependent semi-circle. The measured non-linear behavior of the positive electrode is illustrated in Fig. 9 (left hand, "$R_{\text{pos\_2}}$ (spectra)") and can be explained by a Butler–Volmer behavior. Also given is the current-dependent behavior of the first semi-circle of the negative electrode. It corresponds to an already observed characteristic [1] and can be modeled by a phenomenologically assumed tanh-function. The behavior of the negative electrode at lower f_{ac} is determined by a second "circle" which reaches the positive imaginary region. This part of the spectrum has been ignored in the parameterization of the model.

According to the spectra and the above mentioned processes, a complex model structure has been developed (Fig. 10). The electrodes are completely separated from each other. The dynamic behavior of both electrodes is considered by *RC* elements with partly non-linear resistors. Actually, the quiescent electrode potential should be connected in parallel to the double layer capacitance and in series with the charge transfer resistance. Since a clear identification of both effects is not possible (each electrode provides two *RC* elements), the quiescent potential has been connected in series with the *RC* elements. Nevertheless, the dynamic behavior is not influenced by this simplification. Also, the overcharging models have been employed by two voltage sources $E_{\text{Pb}^{2+}\text{pos}}$ and $E_{\text{Pb}^{2+}\text{pos}}$ whose values are calculated according to Eqs. (1) and (2). The secondary reactions are considered as illustrated above.

5.2. Parameterization of the model

Detailed information on the impedance-based parameterization procedure of the *RC* elements and the time-domain parameterization of the electrolyte transport model can be found in the literature [1,2]. The parameterization of the *RC* elements is based on galvanostatic impedance measurements using several bias dc-currents at different SOC and temperatures. Thus, the non-linear dynamic behavior of the battery can be determined.

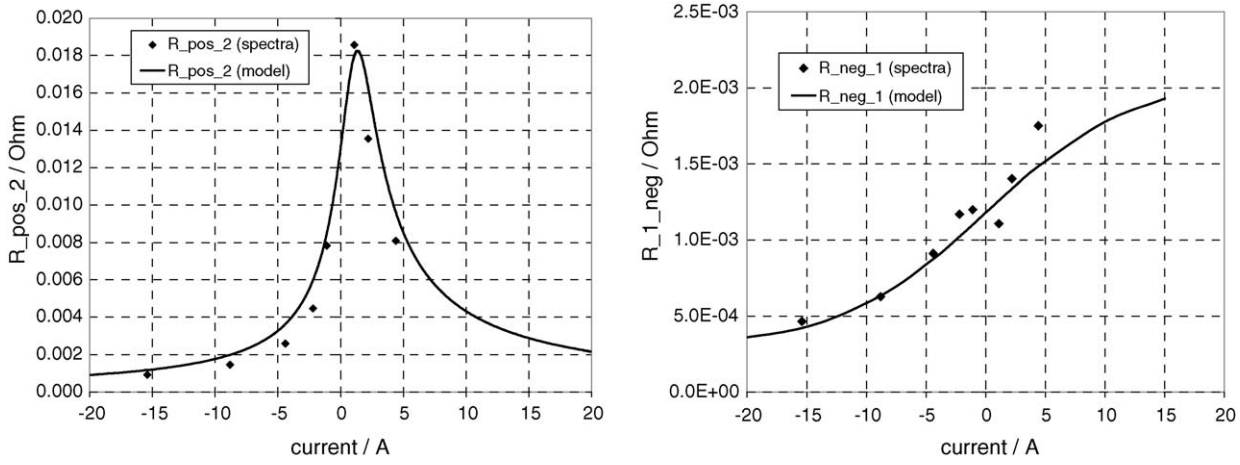

Fig. 9. Non-linear behavior of the electrodes (70% SOC at room temperature); "spectra"-values are extracted from measured impedance spectra, "model"-curves correspond to a Butler–Volmer behavior (positive electrode) and a phenomenologically modeled behavior (negative electrode).

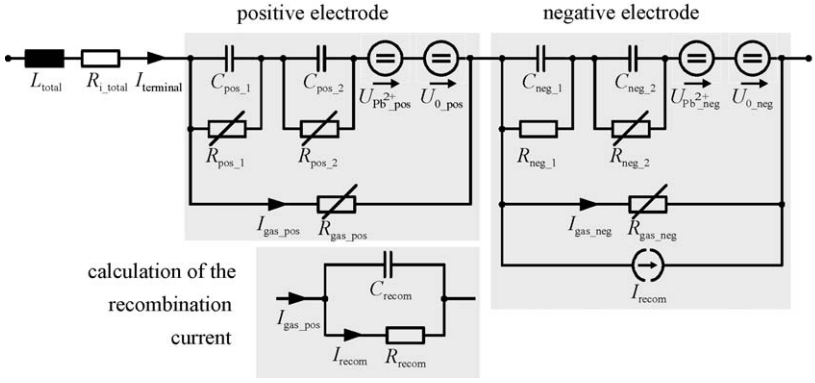

Fig. 10. The complete battery model topology with separated electrodes.

The parameterization of the transport model consists of the evaluation of defined discharging steps at several SOC.

An effective parameter D_{eff} could be derived for a ramp distribution of the sulfate crystals size (Eq. (20)). This parameter has been parameterized for different states of charge (60, 70 and 90%) using alternating charging and discharging steps. The current value has been increased until overcharging effects could be identified, respectively, the maximum accepted charging current has been found (see Fig. 11, left hand). The parameter D_{eff} is given in Fig. 11 (right hand). Since only the values at 60, 70 and 90% SOC have been determined, the remaining values are extrapolated.

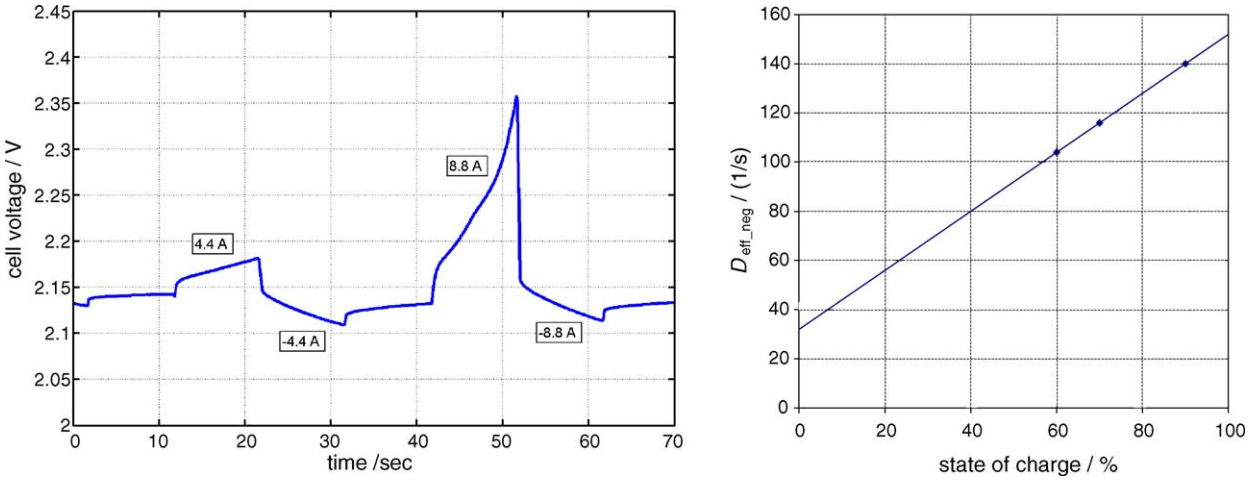

Fig. 11. Cell voltage during alternating charging and discharging steps at 90% SOC with 10 s duration, begin of overcharging effects at 8.8 A ($4 \times I_{20}$) (left hand); effective parameter D_{eff} determined at 60, 70 and 90% SOC, all remaining values are linearly inter- and extrapolated (right hand).

For the parameterization of the gassing model, different constant currents have been applied to the fully charged battery. The resulting potentials of the single electrodes have been measured after a minimum of a 24 h period whilst applying a constant current (Fig. 12). The positive electrode shows an almost exponential behavior, whereas the negative electrode is characterized by two different effects dependent on the level of the applied current. For lower currents, sufficient oxygen can be transported to the negative electrode and the applied current is consumed for oxygen reduction. The electrode is depolarized. For higher currents, the applied current is not only consumed for oxygen reduction but also for hydrogen generation. The negative electrode polarizes. The parameterized modeling of the secondary reactions is given with solid lines. The generally known slopes of oxygen and hydrogen generation are depicted with dashed lines. Further information can be found in [17].

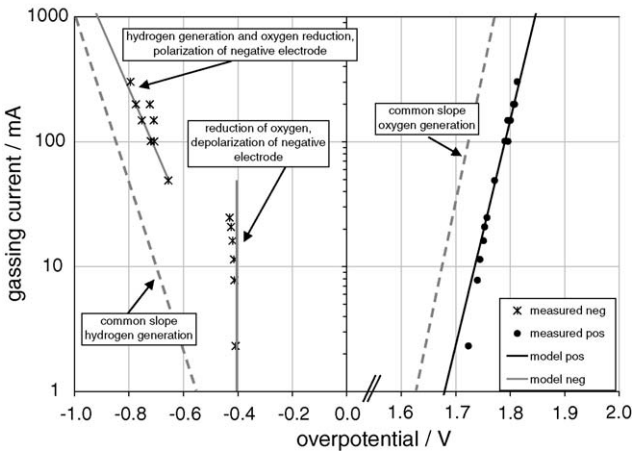

Fig. 12. Overpotential of negative and positive electrode related to hydrogen reference-electrode; solid lines: modeling of gassing behavior (VRLA battery), dashed lines: Tafel slopes according to literature [10].

6. Simulation results

For verification, a dynamic current profile with alternating pulses (10 s duration) and rest periods in between has been applied. Values from ±2.2 to ±61.6 A have been used which correspond to multiples of the nominal battery current $I_N = I_{20} = 2.2$ A ($1 \times I_{20}$ to $28 \times I_{20}$). The verification has been carried out using a voltage limitation at 2.43 V/cell. A PID controller has been added to the simulation model, so that the battery current has been controlled during the voltage limited charging

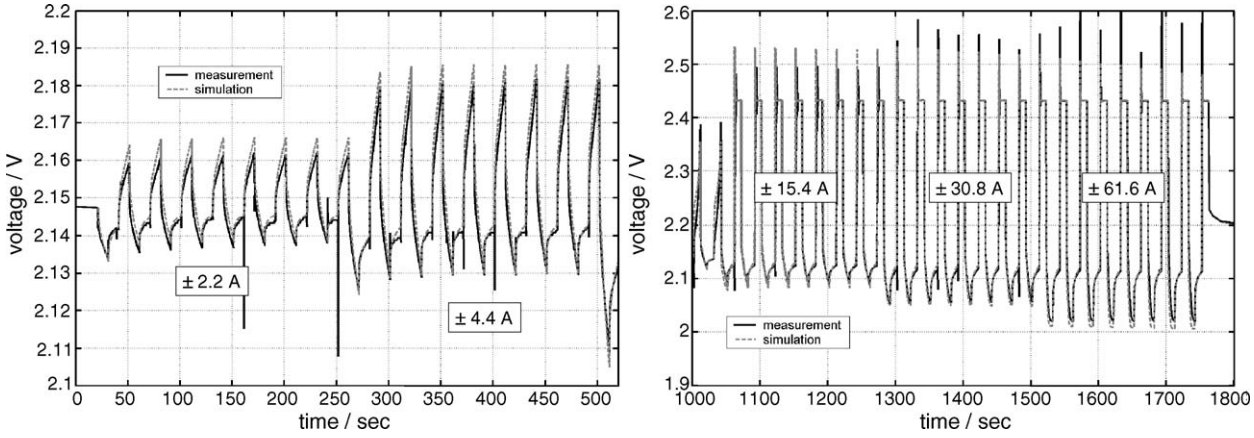

Fig. 13. Simulation and measurement data at 90% SOC, repetition of several current steps with ±2.2 A up to ±61.6 A current value, charging periods are voltage limited at 2.43 V (red-top Optima battery, 12 V, 44 Ah).

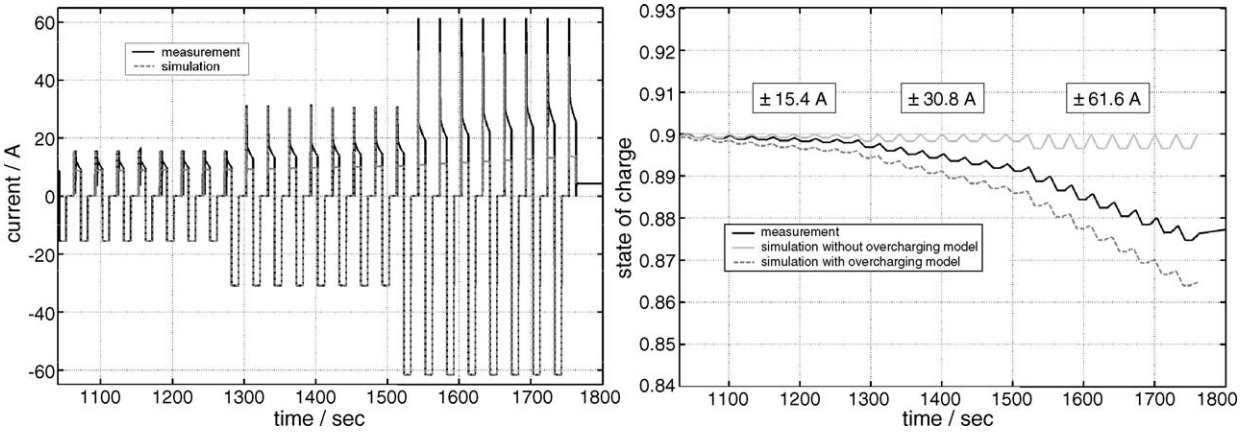

Fig. 14. Left hand: measurement and simulation of battery current during constant voltage charging without "hardening crystals" concept corresponding to Fig. 13; right hand: comparison of SOC calculations ("measurement": integration of the measured terminal current (red-top Optima battery, 12 V, 44 Ah)).

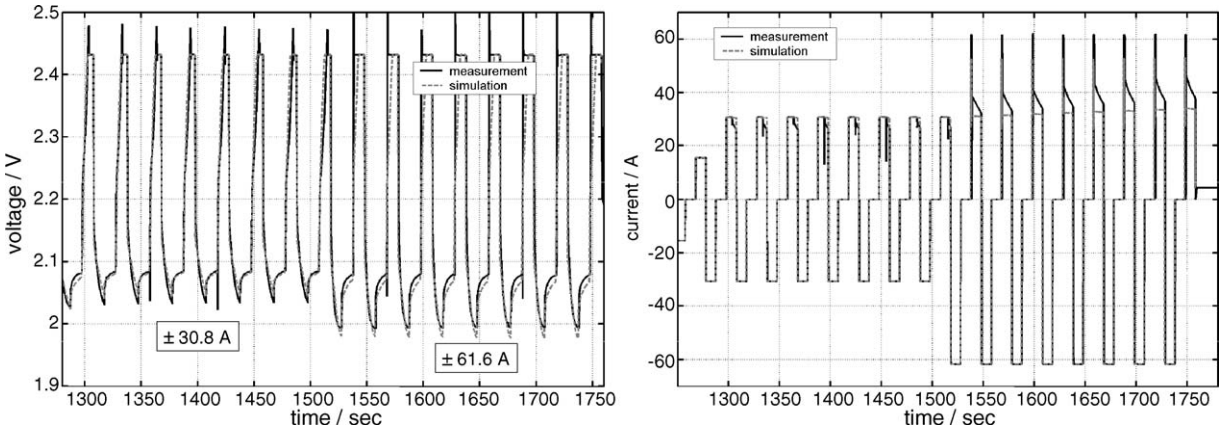

Fig. 15. Measurement and simulation results at 70% SOC and room temperature (red-top Optima battery, 12 V, 44 Ah), repetition of current steps with ±30.8 and ±61.6 A current value, charging periods are voltage limited at 2.43 V (left hand); battery current during the constant voltage charging periods without "hardening crystals" concept (right hand).

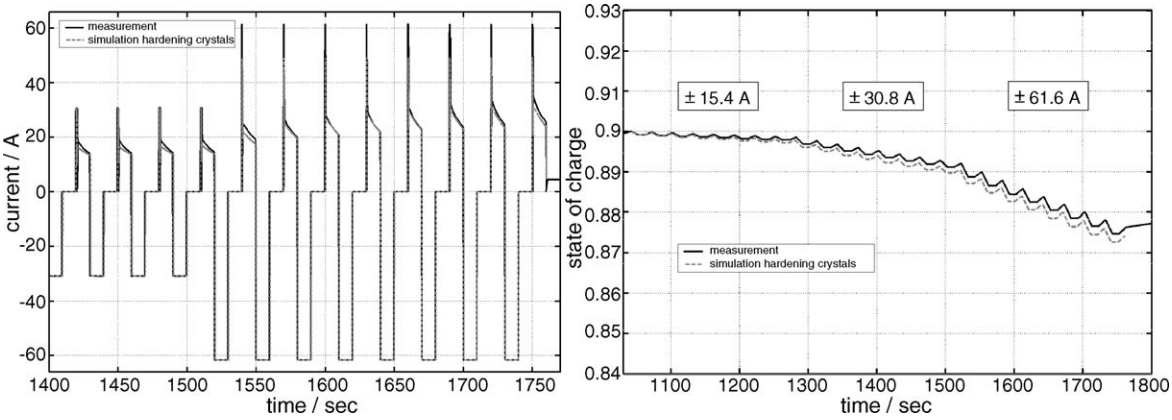

Fig. 16. Left hand: simulated and measured current during constant voltage charging corresponding to Fig. 14 but using the "hardening crystals" modeling approach; right hand: significantly improved SOC calculation.

periods. This procedure is very similar to battery charging equipment during constant voltage charging. Thus, the simulated and measured voltages during the limitation are equal and, for verification of the model, the controlled currents have consequently also to be compared during the voltage limitation.

Initially, the measured and the simulated voltage responses are compared at 90% SOC (Fig. 13). In spite of the very high resolution, only slight deviations become obvious (<10 mV). The left hand figure illustrates the first two different current values (±2.2 and ±4.4 A) whereat the voltage limitation is not reached. The figure on the right hand gives the results of the last three current values (±15.4, ±30.8 and ±61.6 A). Both, the measurement and the simulation reach the voltage limitation.

Moreover, the controlled currents are compared in Fig. 14 (left hand). Without modeling the mentioned "hardening crystals" effect, the overcharging model is only dependent on SOC. Thus, the simulated current shows no dependency on the battery current history (e.g. no dynamic behavior can be observed during the 10 s charging steps). Nevertheless, the use of an overcharging model (even though dependent on SOC only) limits the charge acceptance at all and improves the SOC calculation consequently (right hand).

The same verification profile has been applied to the battery at 70% SOC. Again, only negligible deviations between the simulated and the measured voltages are observable (Fig. 15). The deviations of the battery currents during the constant voltage charging periods (again without using the concept of "hardening crystals") are smaller, but qualitatively the same as detected at 90% SOC.

Finally, the current deviations can be minimized by the employment of the "hardening crystals" approach. Fig. 16 illustrates the results at 90% SOC corresponding to Fig. 14. Both, the absolute value of the accepted charging current, which grows with increased discharging current in short-term history, and the dynamic behavior during the charging steps can be simulated nearly analog to measurement data. The SOC calculation is improved accordingly.

7. Conclusions and summary

A significantly improved modeling approach for lead-acid batteries has been illustrated. Primarily, the overcharging processes have been discussed and useful mathematical approaches have been given for modeling. Finally, the concept of "harden-

ing crystals" has been identified as an important prerequisite for the simulation of the batteries charge acceptance. The concept validation has been performed by using measurements on a VRLA/AGM battery.

However, more theoretical explanation and experimental evidence for the "hardening crystal" concept would be beneficial for the understanding and adequate parameterization. Moreover, simplifications regarding the model topology and the parameterization process are imaginable particularly for flooded lead-acid batteries. Since the recombination process is negligible there, the separation of both electrodes is not absolutely necessary anymore. The gassing and a overcharging model for both electrodes could be merged, removing the need for reference-electrode measurements. The simplified model structure (Fig. 1, right hand) could be reused.

References

[1] S. Buller, M. Thele, E. Karden, R.W. De Doncker, J. Power Sources 113 (2003) 422–430.
[2] M. Thele, S. Buller, D.U. Sauer, R.W. De Doncker, E. Karden, J. Power Sources 144 (2005) 461–466.
[3] D.U. Sauer, J. Garche, J. Power Sources 95 (2001).
[4] W. Kappus, Electrochim. Acta 28 (1983) 1529.
[5] D. Berndt, J. Power Sources 100 (2001) 29–46.
[6] D. Berndt, Maintenance Free Batteries, ISBN 0-863-80198-6.
[7] D.U. Sauer, Optimierung des Einsatzes von Blei-Säure-Akkumulatoren in PV-Hybrid-Systemen unter spezieller Berücksichtigung der Batteriealterung, Ph.D. thesis, University of Ulm, 2003.
[8] J.O'M. Bockris, A.K.N. Reddy, M. Gamboa-Aldeco, Modern Electrochemistry, second ed., Fundamentals of Electrodics, vol. 2A, Kluwer Acad., 2000, p. 1425.
[9] J.R. Macdonald (Ed.), Impedance Spectroscopy, Emphasizing Solid Materials and Systems, ISBN 0-471-83122-0.
[10] H. Bode, Lead-Acid Batteries, ISBN 0-471-08455-7.
[11] P. Mauracher, E. Karden, J. Power Sources 67 (1997) 69–84.
[12] E. Barsoukov, J.H. Kim, C.O. Yoon, H. Lee, J. Power Sources 83 (1999) 61–70.
[13] S. Buller, Impedance-based simulation models for energy storage devices in advanced automotive power systems, Ph.D. thesis, RWTH Aachen University, 2002.
[14] H. Andersson, I. Petersson, E. Ahlberg, J. Appl. Electrochem. 31 (2001) 1–11.
[15] A.J. Salkind, P. Singh, A. Cannone, T. Atwater, X. Wang, D. Reisner, J. Power Sources 116 (2003) 174–184.
[16] N. Abolhasani, N. Gharib, H. Moqtaderi, M. Amin, F. Torabi, A. Mosahebi, M. Hejabi, Prediction of SOC effects on lead-acid battery characteristics using neural network parameter modifier, in: Proceedings of the 6th LABAT, Varna, Bulgaria, June 2005.
[17] A. Hammouche, M. Thele, D.U. Sauer, Analysis of gassing processes in VRLA/spirally wound battery, in: Proceedings of the 6th LABAT, Varna, Bulgaria, J. Power Sources, June 2005, accepted for publication.